Version of Record: https://www.sciencedirect.com/science/article/pii/S001910351830438X
Manuscript_8b5c13c3b8eb4e1c0eb20c0349de4107

Retrieval of the water ice column and physical properties of water-ice clouds in the Martian atmosphere using the OMEGA imaging spectrometer

K. S. Olsen[a,b,*], F. Forget[a], J.-B. Madeleine[a], A. Szantai[a], J. Audouard[b], A. Geminale[c], F. Altieri[c], G. Bellucci[c], F. Oliva[c], L. Montabone[a,d], M. J. Wolff[d]

[a] *Laboratoire de Météorologie Dynamique (CNRS/UPMC/IPSL), Paris, France.*
[b] *Laboratoire Atmosphères, Milieux, Observations Spatiales (CNRS/IPSL), Guyancourt, France.*
[c] *Istituto di Astrofisica e Planetologia Spaziali (IAPS/INAF), Rome, Italy.*
[d] *Space Science Institute, Boulder, USA.*

Abstract

Using spectral images recorded by the OMEGA instrument on Mars Express (Observatoire pour la Minéralogie, l'Eau, les Glaces et l'Activité), we are able derive physical properties of aerosols in water-ice clouds on Mars for a distribution of pixels over an observed cloud formation. These properties, mean effective radius, r_{eff}, and optical depth (at 0.67 µm), τ_{i}, were used to estimate the water ice-column (WIC), and we found an empirical relationship between the WIC and an ice cloud index (ICI). The overall mean of retrieved

*Corresponding author
Email addresses: kevin.olsen@latmos.ispl.fr (K. S. Olsen), francois.forget@lmd.jussieu.fr (F. Forget), jean-baptiste.madeleine@lmd.jussieu.fr (J.-B. Madeleine), szantai@lmd.polytechnique.fr (A. Szantai), joachim.audouard@latmos.ipsl.fr (J. Audouard), anna.geminale@iaps.inaf.it (A. Geminale), francesca.altieri@iaps.inaf.it (F. Altieri), giancarlo.bellucci@iaps.inaf.it (G. Bellucci), fabrizio.oliva@iaps.inaf.it (F. Oliva), lmontabone@spacescience.org (L. Montabone), mjwolff@spacescience.org (M. J. Wolff)

r_{eff} is $\sim 2.2\,\mu\text{m}$, with a standard deviation of 0.8µm, and cloud formations with r_{eff} between 4.4 and 5.4 µm are observed. The optical depth varies between 0.2 and 2.0. The OMEGA spectra are primarily sensitive to water ice mass due to absorption, and we find that the ICI, very easy to compute, is a good proxy for the mass of the water-ice column (WIC) along the optical line of sight. Our retrieval of physical properties is limited in time (to before 2010) by the exhaustion of coolant for one of the OMEGA channels, and in space (to equatorial observations between 140°W–90°E) by the availability of surface albedo measurements. However, we used the ICI to compute WIC values for the entire OMEGA data set, which has near-global coverage for Mars years 26–32, and we present a climatology of the WIC derived from the OMEGA data, which features enhancements on the order of 1.2–1.6 pr. µm over the aphelion cloud belt, and 1.5–2.5 pr. µm over the polar hoods. The data set analyzed is for observations between 140°W and 90°E, and between 35°S and 35°N. No restriction is placed on season, but the majority of cloudy observations were during the aphelion period from Ls 35° to 135°. This work was motivated by the ability of the OMEGA instrument to observe the distribution of water-ice cloud physical properties, and by the availability of new a priori data sets, especially multi-spectral, aerosol-free surface albedo retrieved from a subset of the OMEGA data featuring a cloud-free sky. The main limitations of the retrieval algorithm are linked to the uncertainties on surface albedo, the dust opacity, and the quantity of water-ice suspended in the atmosphere, which can lead to spectral fits with lower accuracy or unrealistic results. We present distributions of each retrieved parameter, goodness of fit, ICI, and cloud mass, and our investigation of relationships

between each parameter. Our approach was to maximize the amount of data analyzed, apply stringent data quality cuts and take a statistical approach to interpretation.

Keywords: Mars atmosphere, Mars Express, OMEGA, water ice, aerosols, clouds, retrievals, ICI, Climatology

---

1. Introduction

Mars has an active hydrological cycle driven by strong diurnal temperature variations and periodic polar sublimation and condensation activities. Seasonal variations in water content are the result of exchange between different reservoirs, such as polar ice and the atmosphere. Clouds play several important roles in the Martian hydrological cycle, notably influencing interhemisphere transport. In this study, we present the retrieval of physical properties of water-ice particles in Martian clouds: the mean effective radius and optical depth. Observing these properties and understanding their temporal and spatial distribution can lead to improved understanding of several aspects of the Martian hydrological cycle. Clouds and their formation are associated with the changing meteorological state of the atmosphere, temperature, aerosol and water content, and air parcel dynamics. In turn, they affect the radiative state of the atmosphere by modifying its absorptive and reflective properties, as well as its chemical balance through heterogeneous processes (e.g., Haberle et al., 2017, and references therein). Water is considered essential for the emergence of life and its presence on Mars has guided remote sensing and in situ research activities since the planet was first visited. In order to improve our knowledge of the history and habitability of

Mars, we seek to better understand the current climate by identifying and quantifying the water reservoirs, and the exchange of water mass between them, which cloud processes are an integral part of.

The physical properties of water-ice clouds on Mars have previously been measured by instruments on Mariner 9 (Curran et al., 1973; Zasova et al., 2001), Phobos 2 (Petrova et al., 1996), Viking 1 and 2 (Christensen and Zurek, 1984; Tamppari et al., 2003), Mars Pathfinder (Smith and Lemmon, 1999), Mars Global Surveyor (Clancy et al., 2003; Wolff and Clancy, 2003), Phoenix (Whiteway et al., 2009), Mars Express (Zasova et al., 2006; Madeleine et al., 2012; Fedorova et al., 2014), and Mars Reconnaissance Orbiter (Smith et al., 2013; Guzewich et al., 2014) These studies are generally in agreement and observed aerosols with a mean effective radius between 2–3.5 µm. Observations have also been made using the Hubble Space Telescope (James et al., 1996) and from terrestrial observatories (see e.g. Parker et al., 1999; Glenar et al., 2003).

This work follows that of Madeleine et al. (2012) who presented a retrieval technique for estimating the mean effective radius, r_{eff}, and optical depth, τ_{i} (at 0.67 µm), by fitting portions of spectra recorded by the OMEGA instrument (Observatoire pour la Minéralogie, l'Eau, les Glaces et l'Activité) on Mars Express. This paper was motivated by the availability of new prior data sets, which are critical to the accuracy and reliability of the retrieval. Of particular importance are the surface albedos at each wavelength used in the fitting and at the precise locations observed in each pixel. Our objective was to exploit the spatial extent of OMEGA spectral images to investigate the distribution of water ice aerosol physical properties within cloud formations.

Madeleine et al. (2012) examined water-ice cloud formations in the aphelion cloud belt using an ice cloud index (ICI) and analyzed clouds over the Tharsis plateau, seeking diurnal and seasonal trends in particle size and opacity. However, their study was limited to only 14 Mars Express orbits, and the retrieval only used a small subset of OMEGA spatial pixels to represent the cloud formations. Our approach differs from that of Madeleine et al. (2012) in that we have attempted to automate the analysis and retrieve cloud properties from as many pixels as possible, and evaluate the results statistically.

A new method to retrieve multi-spectral surface albedo from OMEGA images using principal component analysis has been used to recreate OMEGA images where each pixel contains the surface albedo as a function of wavelength (Geminale et al., 2015). We have used the ICI to find OMEGA pixels containing clouds that overlap with the available cloud-free, multi-spectral surface albedo maps over the aphelion cloud belt region (between 5° S and 35° N). We have performed retrievals of r_{eff} and τ_{i} on over 200,000 pixels from 94 cloudy OMEGA spectral images that overlap 60 surface albedo maps

The majority of OMEGA observations analyzed have very narrow longitudinal ranges, which makes studying the distribution of r_{eff} difficult. However, r_{eff} and τ_{i} are inversely related and can be used to compute the mass, M, of the water-ice column, which can more directly inform us about daily, seasonal, or geographical trends in their formation. The position of the curve resulting from plotting τ_{i} against r_{eff} varies depending on the ICI of the pixels. These are, in fact, curves of equal mass in the $r_{\text{eff}} - \tau_{\text{i}}$ parameter space. The OMEGA spectra are primarily sensitive to absorption by water-ice aerosols, and therefore to the mass of water-ice along the line of sight. The slope of

the relationship $\tau_{\rm i} \propto 1/r_{\rm eff}$ exhibits an empirical dependence on ICI, and, therefore, we find that the easily-computed ICI is a proxy for water-ice column mass. We observe that the relationship between the two parameters is strongly obeyed, and that within a single cloud formation there can be large variations in the spatial distribution of retrieved $r_{\rm eff}$ values, with corresponding variations in $\tau_{\rm i}$. The cloud mass, however, has a more homogeneous spatial distribution and is similar to that seen in the visible channel of the OMEGA pixels and the ICI maps.

The water-ice column (WIC) is defined as M/ρ and expressed in precipitable (pr.) µm, with ρ being the density of water-ice. We have used the ICI to estimate the WIC for the entire OMEGA data set to produce a multi-year, near-global climatology of water ice aerosols.

After an introduction to the OMEGA instrument and its data product in Section 2, we will introduce the retrieval algorithm in Section 3 and the new prior data sets in Section 4. The subset of OMEGA data used in this study is given in Section 5. Results are presented in Section 6 and will examine the parameter spaces of the retrieved, fixed, and computed variables; the spatial distributions of those variables; seasonal and diurnal trends; the link between water-ice column mass and ICI; and efforts to constrain the retrieval to obtain better performance in the presence of very thin clouds.

2. OMEGA

The OMEGA instrument, on Mars Express, records three-dimensional image cubes where each x-y position contains the reflectance spectrum between 0.35–5.1 µm. The Mars Express orbit is an ellipse with periareion

and apoareion of 298 km and 10,107 km, and OMEGA records images that are 16, 32, 64, or 128 pixels wide, depending on the orbital characteristics at the time, and that may be thousands of pixels long. The spectra are recorded by a 352 detector array in three channels: visible (0.35–1.05 µm), C (1–2.77 µm), and L (2.65–5.1 µm). Spatial resolution of the image cubes depends on the orbital parameters at the time of observation, but they are typically 20–30 km wide for 32 pixels, or 5-7 km wide for 16 pixels (these two cases account for 80% of our data set), but can be several hundred kms wide for 128 pixels. The signal-to-noise is at least 100 and the spectral resolution is generally between 0.013–0.02 µm (Bibring et al., 2004).

Mars Express was launched in June 2003, arrived at Mars in December 2003, began returning OMEGA data in January 2004, and continues to do so, having completed over 14,000 orbits. Unfortunately, instrument degradation over time has led to the death of several pixels, and in September 2010 the coolant supply used by the C channel detectors was exhausted. OMEGA continues to record cubes with the visible and L channels, but our analysis requires the C channel, and so data is limited to 2004–2010, covering three Mars years (MY), in this study.

3. Retrieval Algorithm

The inversion method used here, as described in Madeleine et al. (2012), fits a computed spectrum at seven wavelengths which cover the 1.5 µm, 2 µm, and 3.1 µm water absorption bands. The steps in our analysis are: identifying OMEGA observations with sufficient cloud cover that overlap the OMEGA surface albedo data set, selecting pixels for analysis, matching cloudy pixels

to surface albedo pixels, and performing spectral fitting to retrieve r_{eff} and τ_{i}.

The OMEGA albedo cubes are divided into groups by quadrangle (Batson et al., 1979), and pixel matching was done independently for each group. A bounding box is defined for each group by their latitude and longitude extrema. An OMEGA image cube is selected for pixel matching if a portion of its spatial coverage is within the bounding box, and if the cloud cover is greater than 10%. Cloud coverage is defined as the percentage of pixels in a cube with an ICI of ≤ 0.72. The ICI is defined as the ratio of measured reflectances at 3.4 and 3.52 µm (Langevin et al., 2007), which indicates whether the shape of the 3.1 µm water absorption band reflects the presence of ice. Note that with this definition a lower value means thicker clouds, and the quantity $1 - \mathrm{ICI}$ is also used elsewhere. The threshold value of 0.72 is a qualitative convention adopted by past studies of the ICI (Madeleine et al., 2012; Szantai et al., 2017b, 2019).

For each pixel in a cloudy OMEGA cube, a set of criteria must be met for it to be selected for analysis. The ICI must have been successfully retrieved and be ≤ 0.72. We want to avoid areas with strongly changing brightness features, so the ICI is compared to those of the surrounding pixels. We required that each of the eight surrounding pixels had a successfully retrieved ICI and that the difference between the candidate pixel and each of the surrounding pixels be less than 6%. Smoothing will be implemented by taking the average spectrum with surrounding pixels. To avoid introducing a bias by introducing pixels several times, we also required that no more than three of the surrounding pixels overlap with those of the previously

selected pixel. Finally, the closest pixel in the set of albedo cubes is found. The distance between a candidate pixel and the nearest albedo pixel must be within 1.5 km.

The spectrum to be fitted is the mean of the selected pixel and the eight pixels surrounding it. This reduces instrumental noise, but increases the footprint of the observation being analyzed. The surface albedo is the most critical parameter in the computed spectrum, but the footprint of the observation used to retrieve albedo can already be very large and will not perfectly overlap the footprint of the cloudy pixel being analyzed. The averaging smooths the spectrum, and reduces the effects of small-scale topographical features on reflectance. Our requirement on the similarity of the ICIs of all pixels in the mean improves the likelihood that we are analyzing a homogeneous cloud mass.

Spurious behaviour has been observed in portions of the OMEGA spectral images during different time periods. These pixels are excluded. No orbits after 8485 (MY 30, Ls 135°) are considered due to the loss of coolant in the C-channel detectors. A known misalignment exists between the L- and C-channels during different time periods. This is corrected in both the cloudy OMEGA cubes and the albedo cubes.

The wavelengths in the OMEGA spectra used for the retrieval were chosen to avoid interfering gaseous absorption. A transmission spectrum of the Martian atmosphere in this wavelength region is characterized by several gaseous absorption features (see Madeleine et al. (2012)) which can be excluded from the fitting to reduce the number of parameters fit and avoid steps taken to correct for gaseous absorption, which both result in reduced

uncertainties. The detectors for two of the wavelengths previously used became faulty during later orbits, so we use adjacent wavelengths. This version of the retrieval method computes spectral reflectances at 1.18, 1.49, 1.73, 2.23, 2.43, 3.40, and 3.52 µm (previous pixels included 1.51 and 2.46 µm).

Reflectances are computed using the DISORT radiative transfer code (Stamnes et al., 1988), and the a priori discussed in Section 4: the surface albedo at each wavelength retrieved from a cloud-free, overlapping OMEGA cube, climatological dust opacity, surface temperature and pressure, and the atmospheric temperature profile. Details about the forward modelling of the computer spectrum and sources of error are given in Madeleine et al. (2012). The cloud layer is assumed to be at 25 km, and dust is assumed to be uniformly mixed. Single scattering parameters for dust are calculated using the T-Matrix code (Mishchenko et al., 1996), refractive indices from Wolff et al. (2009), and Gamma size distribution with $r_{\mathrm{eff,d}} = 1.5\,\mu\mathrm{m}$, $\nu_{\mathrm{eff,d}} = 0.3$, as recommended by Wolff et al. (2009). For water ice, single scattering parameters are deduced from Mie theory, refractive indices are taken from Warren and Brandt (2008), and a log-normal distribution of effective variance, ν_{eff}, of 0.1 is used. The computed spectrum is then fitted to the measured spectrum, with r_{eff} and τ_{i} as free parameters. Minimization is done using a Levenberg-Marquardt least squares routine. An example OMEGA spectrum and corresponding surface albedo and best fit are shown in Fig. 1a. Fig. 1b shows the water absorption features present in the OMEGA data by comparing a spectrum obtained in the presence of clouds, and the corresponding cloud-free spectrum used to retrieve surface albedo.

The retrieval of water-ice cloud properties from the OMEGA image cubes

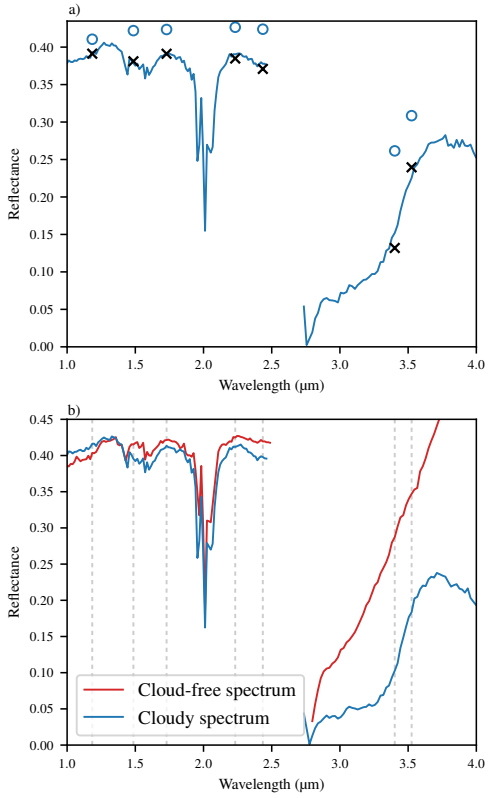

Figure 1: a) An example OMEGA spectrum and best fit for a single selected pixel. Shown are the spectrum, in blue, from the C channel (1–2.6 µm) and L channel (2.6–4 µm); the a priori albedo, blue circles; and the best fit results, black ×. b) Comparison of two OMEGA observations of the same location for periods when water ice clouds were present, blue, and when the region was cloud free, red, and the spectrum was used to retrieve surface albedo.

is very difficult and not always successful. The majority of clouds observed are too optically thin for significant water-ice absorption features to appear in the spectra. The OMEGA instrument has limitations for this sensitive application, such as a narrow spectral range, coarse spectral resolution, and a noise level that is significant relative to the water-ice features. The retrieval

depends on several a priori parameters which are uncertain. Errors made in each a priori parameter will propagate to the retrieved values of r_{eff} and τ_{i}. Of critical importance are the retrieved albedo values. Our retrieval is most sensitive to this parameter. Note, however, that both the surface albedo retrieval and the cloud properties retrieval use the same source data for the dust optical depth. Changing the a priori dust optical depth, atmospheric temperature, or surface temperature results in small changes in the results. Varying the albedo, however, can result in non-convergence.

In Fig. 2, we show the distribution of χ^2 values (see Madeleine et al. (2012) for details) resulting from a range of r_{eff} and τ_{i} values for two spectra, for which we found retrieved r_{eff} values of 3.8 µm (panel a) and 7.6 µm (panel b). The higher retrieved r_{eff} value is associated with a lower optical depth. The curves visible in both panels show allowed r_{eff} and τ_{i} combinations for an equal water ice column mass. The OMEGA instrument is sensitive to the mass of water ice and any errors made in the retrieval of r_{eff} and τ_{i} will still reflect the mass of the column. Combinations of r_{eff} and τ_{i} that lie far from this curve (e.g., large particle sizes and optically thick clouds) cannot be used to accurately model an OMEGA spectrum. The relationship between r_{eff} and τ_{i} is discussed in sections 6.2 and 6.3.

We also see that the regions of low χ^2, where good spectral fits and likely solutions are found, tend to be large areas where several possible solutions can produce reasonable fits. For optically thin clouds, with low τ_{i} values, these regions can be broad, but still follow a curve of equal mass in the parameter space, as shown in Fig. 2b. For retrievals with $\tau_{\mathrm{i}} \lesssim .4$ a wide range of r_{eff} values produce reasonable fits, and the minimization can find

best-fit solutions with r_{eff} values greater than our expectations of 2–5 µm, which are based on past observations such as those shown in Fig. 4c.

A large effort was made to understand what causes these high-r_{eff} retrievals and whether they were reliable and properly representative of the state of the atmosphere. This effort is discussed in Section 7. This type of solution is highly degenerative and occurs only for thin clouds when the water-ice absorption in the spectrum is weakest. Small errors in our signal (e.g., noise) or our model (e.g., errors in a priori) can lead to large errors in r_{eff}. Often, these results will occur within a cloud formation alongside retrieved r_{eff} values of $\sim 3\,\mu\text{m}$, such as those shown in Fig. 6c, while we do not expect such extreme variation in r_{eff} within a single formation. However, we also find cloud formations predominantly made up of large particles, as shown in Section 7 (Fig. 12a). We have identified conditions that preferentially cause high-r_{eff} results, but we do not discount this data, as it may be real in some cases, and there are exceptions to any rule for data rejection. Instead, we present the full set of retrievals, pushing the limitations of our data and method, and urge caution when interpreting retrievals of $r_{\text{eff}} \gtrsim 10\,\mu\text{m}$, which may be viable in some instances.

4. Prior Information

The retrieval algorithm requires accurate prior knowledge of the surface albedo at each fitted wavelength, the surface temperature the surface pressure, the vertical profiles of atmospheric pressure and of temperature, and the opacity of atmospheric dust. To select pixels for analysis, we also require the ICI. To aid studies of the cloud cover on Mars, pre-computed ICI maps

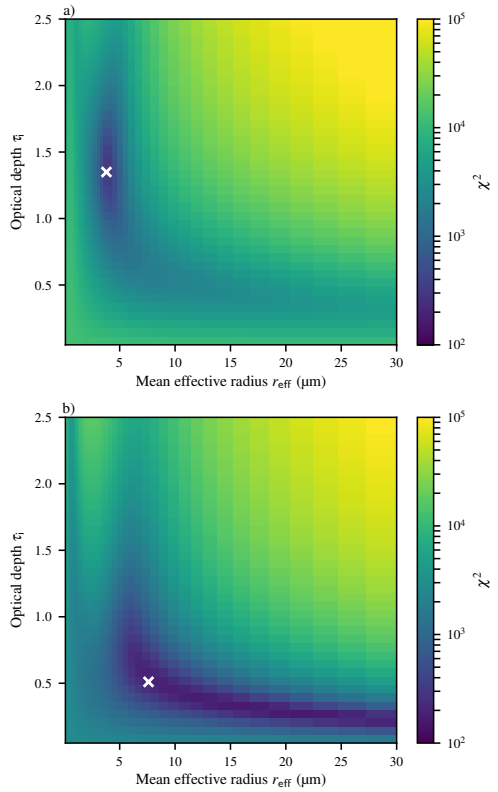

Figure 2: The distribution of χ^2 values for two OMEGA spectra with features that result in retrievals of: a) $r_{\text{eff}} = 3.8\,\mu\text{m}$ and $\tau_{\text{i}} = 1.35$; and b) $r_{\text{eff}} = 7.6\,\mu\text{m}$ and $\tau_{\text{i}} = 0.51$. The χ^2 minimization results are shown with white $\times$.

have been created for the entire OMEGA data set, along with a database of parameters and statistics (such as percent of pixels with water ice cloud cover) for each OMEGA cube (Szantai et al., 2017a).

To obtain the temperature of the surface and atmosphere for each pixel, we used the latest version of the LMD Mars general circulation model (LMD-GCM) (Forget et al., 1999) accessed through the Mars Climate Database (MCD) V5.2 (Millour et al., 2015). Madeleine et al. (2012) computed the ICI

for each analyzed pixel at the time of the retrieval and used an older version of the MCD (V4.3) to obtain temperature information. The more recent version of the MCD reflects significant improvements in the modelling of the main atmospheric cycles on Mars, such as dust, water, and CO_2, due to large improvements in the LMD-GCM, such as the inclusion of radiatively active clouds (Madeleine et al., 2012), semi-interactive dust transport, and new dust radiative properties (Madeleine et al., 2011). Other improvements were made to the cloud micro-physics (Navarro et al., 2014), convective boundary layer scheme, CO_2 cycle, and the representation of non-local thermodynamic equilibrium cooling in the upper atmosphere.

To get the atmospheric dust content, Madeleine et al. (2012) scaled the measurements from the nearest Mars Exploration Rover on the day of the observation, which would have been thousands of km away, assuming that dust was uniformly mixed horizontally and vertically. A new climatological database of dust opacities has been developed using observations from the Mars Global Surveyor Thermal Emission Spectrometer (TES), the Mars Odyssey Thermal Emission Imaging System (THEMIS), and the Mars Reconnaissance Orbiter Mars Climate Sounder (MCS), and including observations from the Martian surface when available (Montabone et al., 2015). In our analyzed data set, there are no directly coincident dust measurements in the database, so we used the complete-coverage reconstructed maps (kriged data rather than gridded). In order to use the data in our retrieval algorithm, several steps were taken: the dust column provided is at a constant pressure level, and we correct to the surface pressure and elevation of each pixel location; the data provided are absorption optical depths and we re-

quire extinction optical depths, so they are converted by multiplying by a factor of 1.3 (Wolff and Clancy, 2003); the data provided are at 9.3 µm, and we require the optical depth at 0.88 µm, obtained by multiplying by a factor of 2.0 as recommended by Montabone et al. (2015). These approximations introduce non-negligible uncertainties into the dust content used by both the surface albedo retrievals and cloud properties retrievals.

In order to retrieve cloud properties from OMEGA spectra, Madeleine et al. (2012) first searched for a cloud-free OMEGA spectrum at the same location. A strict set of criteria were applied to the selection of a cloud-free spectrum, restricting the slope of the ground, difference in dust content between the cloud and cloud-free spectra, and the difference in their observation angles. The cloud-free spectrum was first used to retrieve the surface albedo using spectral fitting between the observed spectrum and a spectrum computed using the DISORT radiative transfer code (Stamnes et al., 1988) using the surface albedo as the free parameter. A priori information for the cloud-free spectrum came from the same sources as for the cloudy spectrum.

Geminale et al. (2015) have analyzed a subset of OMEGA image cubes to retrieve surface albedo for each wavelength of the OMEGA spectra. Their retrieval method uses a combination of principle component analysis and target transformation to remove the gaseous atmospheric contribution to the OMEGA spectra in the spectral range between 0.4–4 µm. Their aim is to remove the spectral components produced by the atmosphere to improve studies of Martian surface mineralogy. The covariance matrix for a set of OMEGA spectra is used to derive a set of eigenvectors which are transformed into a set of spectral end-members that can be used to reproduce the

observed spectra. A spectrum of the surface reflectance is constructed from a linear combination of spectral end-members with those attributed to the gaseous atmospheric contribution removed. Moreover, the dust contribution has been removed by the spectrum considering that the observed reflectance factor at a given wavelength is a function of surface reflectance and dust optical depth (Vincendon et al., 2007). Taking advantage of this relationship and using dust opacities from Montabone et al. (2015), it is possible to simulate reflectance factors using a multiple-scattering radiative transfer code (Ignatiev et al., 2005). The surface reflectance factor is determined as the value that corresponds to the best fit between the observed reflectance factor and simulated one for each wavelength. Finally, the surface thermal contribution is removed in the spectral range between 3–4 µm (Audouard et al., 2014). It should be taken into account that the surface spectra retrieval strongly depends on the assumptions made on dust (grain size distribution, radius, and variance) and on the dust optical depth values. Indeed, dust properties could depart from the ones assumed in the model and this can be even more important when dust optical depth is high. This is the same conclusion reached by Madeleine et al. (2012).

In their original publication, Geminale et al. (2015) analyzed two OMEGA image cubes, but have since expanded their data set. We used 60 multispectral albedo cubes in this study. A comparison of the albedos retrieved by Madeleine et al. (2012) and by Geminale et al. (2015) is discussed in Section 6 and shown in Fig. 4. Using the ICI as an indicator, and considering the fraction of pixels with an ICI less than 0.72, 55 of the 60 OMEGA image cubes are cloud free, and four of them have cloud cover over less than 0.3%

of their area. The remaining one cube has a cloud fraction of 9%, but none of the overlapping pixels used from this cube bore clouds. Dust affects the accuracy of the albedo retrieval and can impact cloud properties retrievals. This is discussed in Section 7.

5. Data Set

The OMEGA data were produced in groups and cover the Mars quadrangles MC09 (Tharsis) to MC13 (Syrtis Major). This region stretches from 140°W to 90°E and from 35°S to 35°N. The coverage of the albedo data is presented in Fig. 3, which shows the surface albedo at 1.51 µm. From these 60 albedo cubes, we found 94 cloudy OMEGA image cubes with overlapping pixels suitable for analysis. Table 1 gives a summary of the number of pixels analyzed over each region, and shows that the highest number were found over the Tharsis region, where the extreme topography of the Tharsis volcanoes drives cloud formation. In total, we analyzed 209,936 pixels, with 158,190 coming from the MC09 and MC17 regions.

No restriction was places on Ls, but the majority of cloudy observations found come from the aphelion period, between Ls 35° and Ls 135°. The distribution of observations has two peaks near Ls 50° and Ls 100°. There are four observations between Ls 200°–208°, one observation at Ls 12.5°, and another at Ls 351.2°.

A set of data quality cuts were applied to the data to remove poor fits, extreme outliers, and physically unrealistic values. The data have been archived conforming to the Planetary Data System (Version 4) for distribution as part of the UPWARDS project through the ESA Planetary Science Archive at

Table 1: Summary of analyzed pixels from the OMEGA data set showing the locations, Mars quadrangles (MC), number of OMEGA observations used (Obs.), the total number of pixels analyzed, and the number of analyzed pixels passing data quality cuts.

Region	MC	Area	Obs.	pixels	After cuts
Tharsis	09	0°–30°N 90°–135°W	65	142498	100891
Oxia Palus	11	0°–30°N 0°–45°W	20	30771	9203
Arabia	12	0°–30°N 0°–45°E	4	10926	7202
Syrtis Major	13	0°–30°N 45°–90°E	10	10049	6959
Phoenicis Lacus	17	-30°–0°N 90°–135°W	12	15692	5517

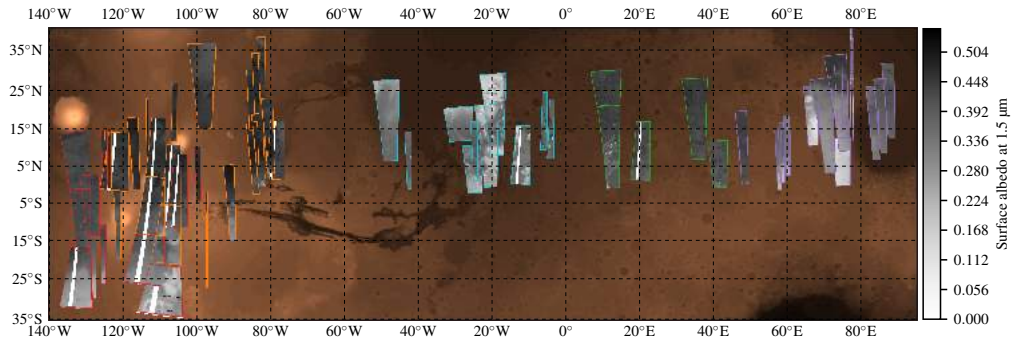

Figure 3: A map of available retrieved surface albedo data, showing the surface albedo at 1.51 µm. The background is a relief of MOLA surface elevation. The outlines indicate the Mars quadrangle, from left to right: MC17 (red), MC09 (orange), MC11 (blue), MC12 (green), and MC13 (violet).

open.esa.int/esa-planetary-science-archive/. The data quality requirements applied are: $\chi 2 < 2000$, $0.5 < r_{\rm eff} < 25$, and $\tau_{\rm i} > 0.15$. The $\chi 2$ requirement affects 49306 (23%) pixels, the requirement imposed on $r_{\rm eff}$ affects 60736 (29%) pixels, and the $\tau_{\rm i}$ requirement affects 6519 (3%) of pixels. Overall, 62% of analyzed pixels passed the data quality cuts. The total number of pixels passing the cuts for each region is given in Table 1. The fitting of 30056 pixels failed to converge, only two thirds of which resulted in $\chi 2$ outside our criterion. Fitting fails to converge when our computed spectrum does not properly model the measured spectrum, which can occur for a variety of reasons that include: errors made in the measurement (e.g., detector degradation over time), a water-ice signal below the instrument noise, or topographic features impacting reflectance (e.g., crater rims). Our investigation into results with good fits, but large retrieved values of $r_{\rm eff}$ is discussed in Section 7.

6. Results

Armed with the new multi-spectral albedo data set, the first thing we examined was the effect the new a priori had on retrievals by comparing them with those presented in Madeleine et al. (2012). We also examined the sensitivity of the retrieval to each piece of a priori information by comparing retrievals after updating only one parameter at a time. What we observed, for 13 of the 14 locations examined in Madeleine et al. (2012) (the fourteenth, orbit 1034_6 (MY 27, Ls 111.9°), had errors in its ICI analysis and so was omitted here), was that changing the a priori dust, surface temperature, or atmospheric temperature vertical profiles caused changes in the retrieved r_{eff} on the order of tenths of µm, with the dust having the largest impact. Two of the locations, in orbits 0887_5 (MY 27, Ls 93.4°) and 1023_6 (MY 27, Ls 110.6°), proved challenging to reproduce the results in Madeleine et al. (2012) with any changes to the a priori. Madeleine et al. (2012) showed that orbit 0887_5 had the highest sensitivity to initial conditions in their study, resulting in the highest uncertainty, while orbit 1023_6 had the lowest water-ice column (WIC), implying the thinnest layer of cloud cover analyzed. We confirm that this pixel also had the highest ICI value within the data set. Finally, changing the a priori surface albedo had a critical impact on the results, causing differences of a few tenths of µm to a few µm in the retrieved r_{eff}.

A comparison of the albedo data retrieved by Madeleine et al. (2012) and Geminale et al. (2015) is shown in Fig. 4, which shows a correlation plot of all the spectral points for the 13 pixels re-analyzed, as well as the mean difference at each spectral point between the albedos retrieved by Madeleine

et al. (2012) and Geminale et al. (2015). We observe a small bias in the results, with those from Geminale et al. (2015) having higher albedos in the C channel region, and much lower albedos in the L channel region. The L channel has the strongest water-ice absorption feature, is the most difficult region of the spectrum to fit, and has a significant impact on the results. It should be noted that the results of (Geminale et al., 2015) also benefit from improvements made to the sources of surface temperature, dust optical depth, and an updated version of the L channel calibration.

Fig. 4 also compares the retrieved r_{eff} results using the new a priori information to those reported in Madeleine et al. (2012) by reproducing Fig. 11a in that paper, which shows r_{eff} as a function of Ls. We find that after updating the a priori, we no longer observe the trend in Fig. 4c discussed in Madeleine et al. (2012), and that some of our results now deviate strongly, illustrating how sensitive and difficult this retrieval is.

In the original analysis of Madeleine et al. (2012), they carefully examined the sensitivity of the retrieval to each piece of a priori information to quantify the uncertainty of their results, and we refer the reader there to further explore the retrieval sensitivity. They obtained uncertainties for retrieved r_{eff} between 0.4–1 µm, as indicated in Fig. 4c, and between 0.09–0.13 for τ_{i}. In all cases, the new apriori data produce better fits for the spectra analyzed by Madeleine et al. (2012). Because of that, and our belief that the new surface albedo is more accurate than before, the uncertainties will be on the same order, but less than those presented by Madeleine et al. (2012). Uncertainties for individual pixel retrievals had not been computed for the entire 200,000 pixel data set at the time of writing due to the unavailability of

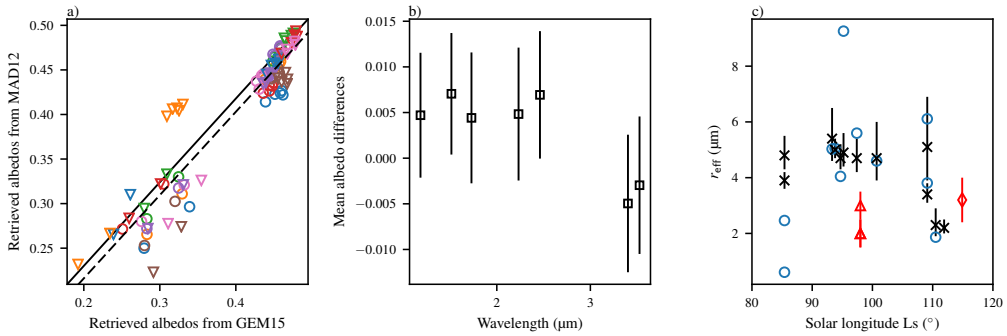

Figure 4: A comparison of the inputs and retrievals presented in Madeleine et al. (2012) and here. Panel a) shows the correlation plot between retrieved aerosol-free surface albedos from Madeleine et al. (2012) and Geminale et al. (2015) (labelled MAD12 and GEM15, respectively). Data shown are for the OMEGA orbits analyzed in Madeleine et al. (2012). Each observation has seven points for each wavelength fit in Fig. 1, and is given a unique colour and symbol combination. Panel b) shows the mean albedo differences at each retrieval wavelength for the same data as in panel a). Panel c) shows the retrieved mean effective radius as a function of solar longitude. Results found for single pixels by Madeleine et al. (2012) are shown in black, and our results, which are the mean of the analysis of many pixels, are shown in blue. Also shown are measurements made by Zasova et al. (2001) (red triangles) and Wolff and Clancy (2003) (red diamond).

rigorously quantified uncertainties in the surface albedo data set, which our calculation is critically dependant on. However, a very good estimate of the uncertainties is determined by considering the ensemble of analyzed pixels, shown in Fig. 5. The standard deviation of retrieved r_{eff} in the primary peak centred near 2 µm is 0.81 µm. The corresponding standard deviation for retrieved τ_{i} is 0.51, indicating that the particle size has less variability than the optical depth.

The objective of this analysis is two-fold: to circumvent the pitfalls of

fitting a single spectrum from a cloud with uncertain a priori information by analyzing a great number of spectra and considering the entire sample of their results; and to explore the variability of water-ice cloud physical properties within a cloud formation.

We have analyzed 94 OMEGA image cubes, with the number of pixels used ranging from a few hundred to several thousand. Fig. 5 presents histograms of r_{eff}, τ_{i}, ICI, and χ^2 for the entire data set, after applying data quality cuts outlined in Section 5. The r_{eff} results are characterized by having two distinct peaks: a tall, narrow peak centred around 2.21 µm (with a standard deviation of 0.81); and a wide, low peak centred around 12.4 µm. (standard deviation of 6.2). Note that the appearance of a minor peak near 5 µm is due to two observations, 0887_5 and 0898_5, with large samples of analyzed pixels and means r_{eff} of 5.2 and 4.7 µm, respectively. These observations were both analyzed by Madeleine et al. (2012) who found similarly large r_{eff} values (5.4 and 4.7 µm). They were recorded on Ls 93.5° and 94.8° in MY 27. Two distinct populations of water ice aerosols were also observed by Wolff and Clancy (2003) and were interpreted to represent distinct cloud types.

These results are in agreement with previous observations and analyses (e.g. Toon et al., 1977; Clancy et al., 1995; Pollack et al., 1995; Wolff and Clancy, 2003), which found water ice aerosol sizes to be around 1–2 µm. Fedorova et al. (2014); Guzewich et al. (2014); Clancy et al. (2003) observed an altitude-dependence in water ice aerosols formed over the aphelion cloud belt, with smaller particles (1–2 µm) forming at higher altitudes, and larger particles (3–4 µm) forming closer to the surface. Smaller particle sizes (0.1 µm)

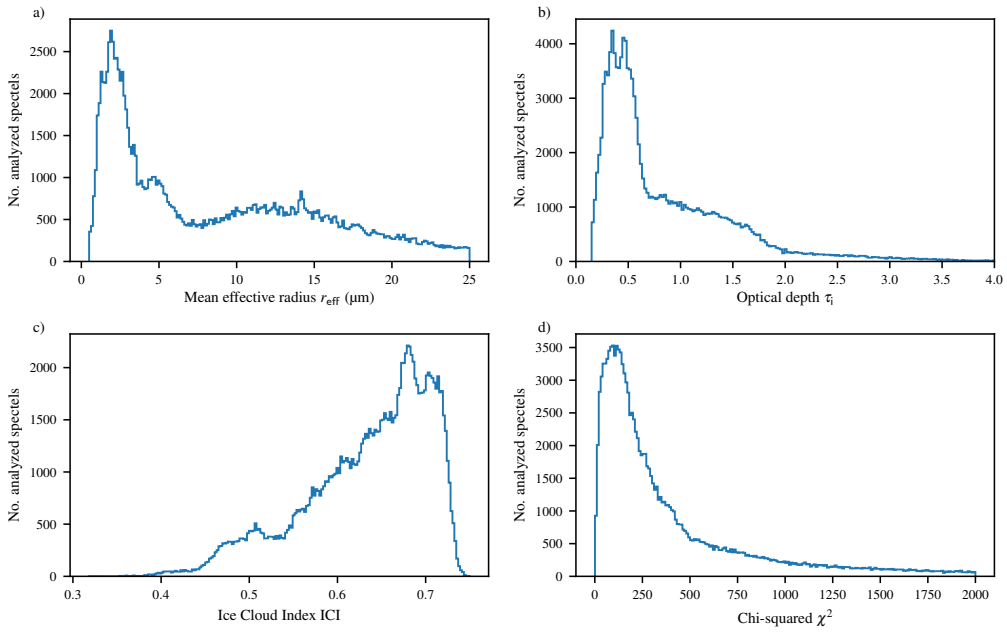

Figure 5: Histograms of: a) retrieved r_{eff}; b) retrieved τ_{i}; c) ICI; and d) χ^2 of the best fit for all analyzed pixels in our data set, after applying data quality cuts.

were also observed by Rannou et al. (2006). Note that τ_{i} is generally less easy to directly compare since it is not always reported at the same wavelength. Madeleine et al. (2012) compares the 0.67 µm τ_{i} retrieved with the method used here to the 0.4 µm τ_{i} reported by Benson et al. (2003), and note agreement within uncertainty.

The τ_{i} results also exhibit a less distinct pair of peaks, with the r_{eff} results above 7 µm corresponding to the τ_{i} results less than 0.6. The relationship between r_{eff}, τ_{i}, and ICI is discussed in sections 6.2 and 6.3, and the results with $r_{\text{eff}} > 7$ µm are discussed in Section 7.

6.1. Spatial Distributions

Our approach to cloud properties retrievals has yielded a data set that allows us to examine the distribution of cloud properties within cloud formations. At this time, however, our data set is limited in size, but also by the viewing geometry of the OMEGA instrument. Fig.s 6 and 7 provide two examples of the mapping of retrieved cloud properties, and show observations from OMEGA orbits 0937_5 (MY 27, Ls 99.7°) and 3272_3 (MY 28, Ls 85.0°), respectively. From left to right they show a visible image derived from OMEGA, the ICI, retrieved r_{eff}, and retrieved τ_{i}, with backgrounds showing the topography and overlapping retrieved surface albedo. The visible images are useful to identify the presence of cloud cover and distinct surface features. A quick comparison of panels a) and b) in both figures highlights the usefulness of the ICI to identify the presence of clouds.

The topography and visible images in panels a) also help evaluate aspects the retrieved surface albedo. The surface albedo does not reflect changes in elevation, but rapid changes in topography, such as craters visible in Fig. 6 and a large cliff band in Fig. 7, appear visible in the albedo data. Since albedo values in these regions reflect physical changes in the surface and in the illumination conditions rather than constant radiometric properties, they prevent accurate cloud properties retrievals. In Fig. 6 there are three large craters. Retrievals were not possible near 9°N, and retrievals resulted in very high estimates of r_{eff} along the crater edges near 10 and 15°N. In Fig. 7, the cliff band near 5°N affects the OMEGA spectra in such a strong way that this feature is visible in the ICI measurements. Cloud properties retrievals in this region result in unrealistically high τ_{i} values.

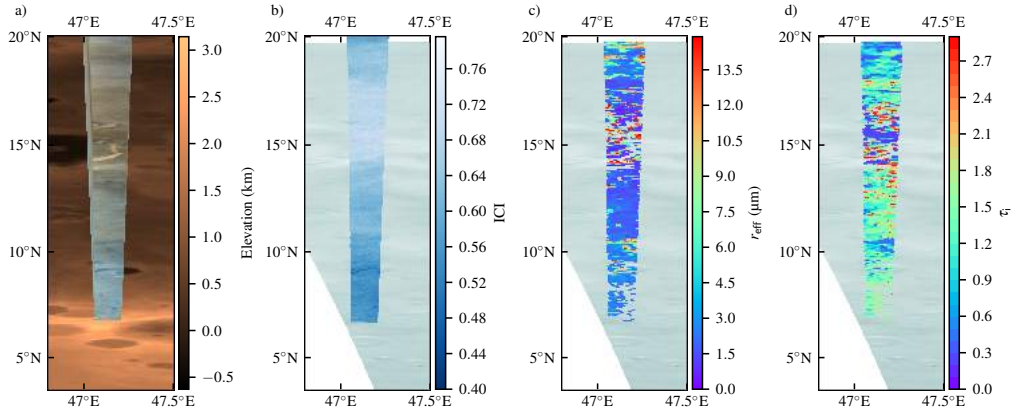

Figure 6: Spatial distributions of retrieved water-ice cloud properties for OMEGA orbit 0937_5 (Ls 99.7, and 16:15 LT). The foregrounds of each panel show the: a) visible image generated from the OMEGA observation, b) the ice cloud index, c) retrieved mean effective radius, and d) retrieved optical depth. The background of panel a) shows MOLA surface elevation, and the backgrounds of panels b), c), and d) show the surface albedo at 1.51 μm retrieved from a co-located cloud-free OMEGA observation.

These figures also illustrate the limitations of the retrieval when cloud thickness, as measured by the ICI, is low. Both figures feature regions with very thin clouds, indicated by high ICI values, where the retrievals result in unrealistic values. This occurs between 15 and 18°N in Fig. 6, where the retrieval found optically thin clouds with very large particles, and between 1 and 3°N in Fig. 7, where the retrieval found optically thick clouds when none were present.

6.2. Cloud Mass

The WIC and water-ice column mass can be computed from the product of the retrieved parameters, r_{eff} and τ_{i} (Mateshvili et al., 2007; Madeleine et al., 2012). Therefore, r_{eff} and τ_{i} are inversely related to one another

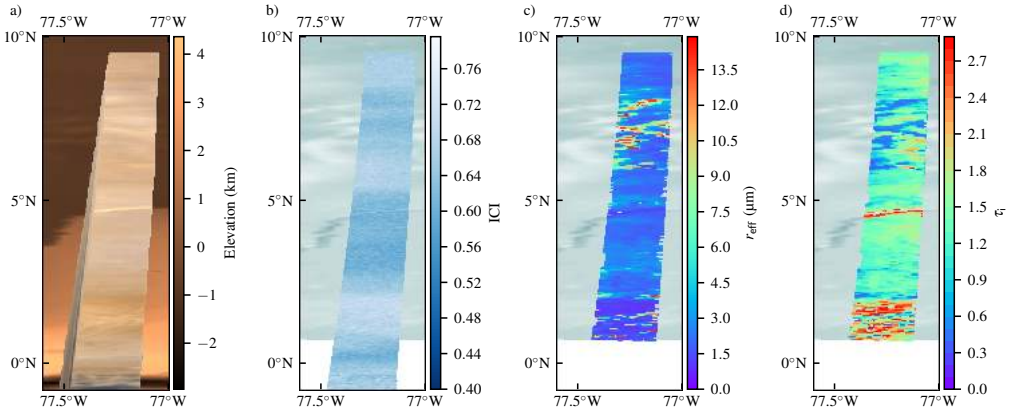

Figure 7: Spatial distributions of retrieved water-ice cloud properties for OMEGA orbit 3272_3 (Ls 85.0, and 14:11 LT). Panels are as in Fig. 6.

through the mass, extinction efficiency, and density of the scattering water-ice aerosols:

$$\tau_{\mathrm{i}} = \frac{3MQ_{\mathrm{ext}}}{4\rho r_{\mathrm{eff}}}, \tag{1}$$

where M is the water-ice column mass along the line of sight, ρ is the density of water ice, and Q_{ext} is the extinction efficiency. A database of Q_{ext} values were pre-computed for range of r_{eff} values using method of Bohren and Huffman (1983) for a log-normal distribution of scattering particles with an effective variance of 0.1, as in Wolff and Clancy (2003) and refractive indices from Warren and Brandt (2008). M is directly proportional to WIC (WIC $= M/\rho$) which was derived from OMEGA retrievals by Madeleine et al. (2012).

Eq. 1 allows us to calculate the column mass of water-ice for each pair of retrieved values. Fig. 8 shows four examples of the spatial distribution of column mass. This is more homogeneous than the individual parameters

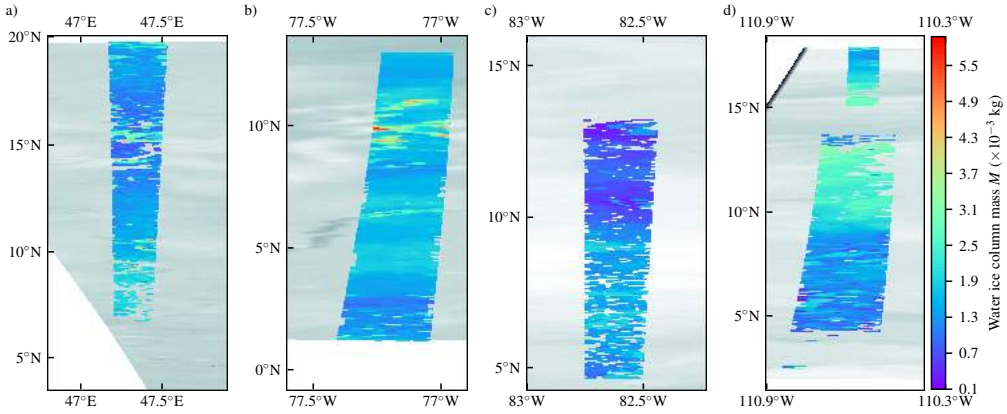

Figure 8: Spatial distributions of retrieved water-ice cloud column mass for OMEGA orbits: a) 0937_5 (Ls 99.7, LT 16:15, MY 27), b) 3272_3 (Ls 85.0, LT 14:11, MY 28), c) 2957_5 (Ls 46.3, LT 16:54, MY 28), and d) 3276_4 (LS 85.5, LT 14.22, MY 28).

and well correlated to the distribution of ICI maps. For example, compare Fig.s 6b and 7b to Fig. 8a and 8b. With the exception of areas around crater edges, we find that the mass distribution is aligned with the ICI distribution, with greater mass correlated to thicker clouds, as expected.

6.3. ICI and Cloud Mass

The relationship given in equation 1 is extremely well obeyed by the cloud properties retrievals from OMEGA observations. This implies that even when a retrieval results in an unrealistic value of r_{eff}, the retrieval is still well enough constrained to obtain a reasonable estimate of water-ice cloud column mass because the cloud spectral signature is primarily controlled by absorption. Fig. 9a shows the relationship between retrieved r_{eff} and τ_{i} values. The colour scale is the ICI and the shapes exhibited by monochromatic bands are curves of equal mass. What we observe is that a retrieval resulting in high mean

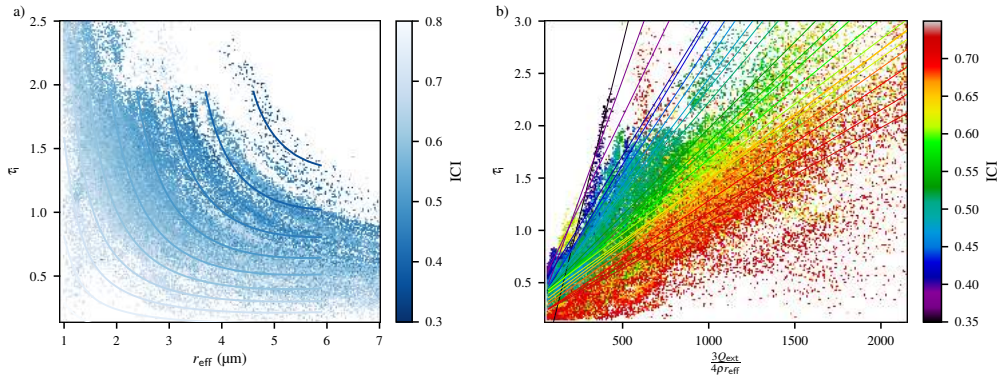

Figure 9: The parameter space of retrieved water-ice cloud properties. Panel a) shows τ_{i} as a function of r_{eff}, with the ICI represented with the colour scale. The contours show ICIs calculated from synthetic spectra generated for the range of r_{eff} and τ_{i} values shown and represent curves of equal mass. Panel b) shows the same data as in panel a) linearized using equation 1. The data was binned according to ICI (each bin represented by a colour) and the slope found. Best fit lines for each ICI are shown, coloured to match the data.

effective radius is always associated with a very low optical depth. We also see a trend in the position of the inverse relationship with ICI, and therefore infer that column mass, M, is be related to ICI. This relationship between r_{eff} and τ_{i} is also exhibited in the χ^2 distributions shown in Fig. 2.

To confirm this relationship we created a model of the r_{eff}–τ_{i} parameter space. For a grid of r_{eff} and τ_{i} values covering the domain and range of Fig. 9a, and a synthetic spectrum was computed at each location. The ICI was found for each synthetic spectrum and the model results are shown in Fig. 9a as contours of ICI. A trend in the contour location with ICI is clearly seen, and the colour scale agrees with the retrieval results. However, the relationship is not exact since the synthetic spectra also depend on surface albedo and the atmospheric dust loading. The model was recreated for several albedo and

dust configurations, and each different scenario alters the contour locations. The spread in the data that have similar ICI values in Fig. 9a is due to variations in those physical parameters.

Fig. 9b presents the data from Fig. 9a in a linearized form, showing the relationship between τ_{i} and $1/r_{\mathrm{eff}}$. The data were grouped into ICI bins (22 bins, widths of 0.019), which are represented by the colours in Fig. 9b, and the slope and intercept of each group were found, with the slope being directly proportional to column mass as in equation 1. The resulting column masses as a function of ICI are shown in Fig. 10. Fig. 10 also shows the results of the same analysis performed for the synthetic data shown in Fig. 9, as well as the distribution of individual retrievals (restricted to r_{eff} values below 7 µm).

What we have found is that the ICI, which is very straight-forward to compute (ratio of reflectances at 3.4 and 3.52 µm), is a good proxy for the column mass of the water-ice aerosols present, or the WIC. Though estimating M or WIC from the resulting relationship shown in Fig. 10 will not be as accurate as performing a full retrieval of r_{eff} and τ_{i}, it is much less computationally expensive and has applications for other data sets. For example, full retrievals of r_{eff} and τ_{i} cannot be made for the entire OMEGA data set due to a lack of retrieved surface albedo data, a lack of suitable overlapping cloud free observations to use for the albedo retrieval, and the relatively short life of the C-channel over the mission duration. This relationship allows us to generate maps of the distribution of M or WIC for the entire OMEGA data set between 2004 to the end of life, when water-ice clouds are present, as determined by the ICI. The primary limitation in this method is that the

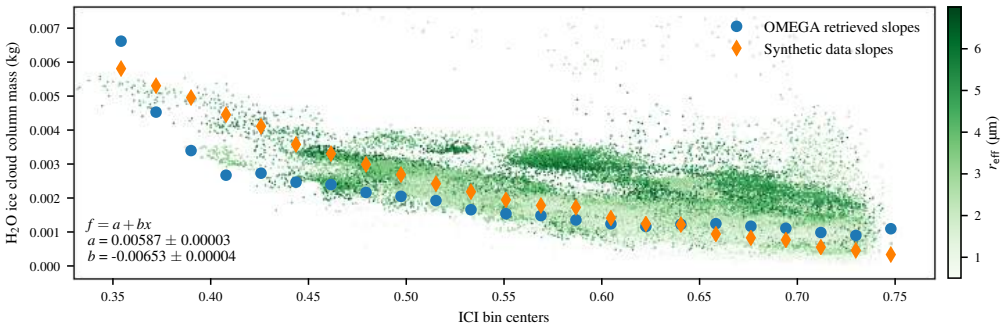

Figure 10: The relationship between water-ice cloud column mass and the ICI. The entire data set, limited to retrievals with $r_{\text{eff}} < 7$ µm, is shown in green, with the colour scale indicating r_{eff} value. The slopes from the binned data in Fig. 9b are shown in blue, as a function of ICI bin centre. The same analysis was performed for the synthetic data shown in Fig. 9a, and its results are shown in orange. Least squares regression results for the r_{eff} – τ_{i} data set are indicated.

distribution of calculated M values will be narrow and will not fully reflect anisotropies in less well constrained parameters such as atmospheric dust opacity and surface albedo.

Regression in the data shown in Fig. 10 is not very well constrained at low ICI and future work will aim to increase the sample size of retrievals from this type of spectra. The slope and intercept given in Fig. 10, -0.00653 and 0.00587, respectively, are the regression statistics for the individual M and ICI values shown. The same analysis has been done for binned data (resulting in $b = -0.009$ and $a = 0.007$),but this is strongly affected by the lack of data below an ICI of 0.4. We also fit various curves to the data, but this leads to unrealistically high and poorly constrained results at low-ICI.

We have used this relationship to estimate the WIC for the entire available

OMEGA data set covering Mars years 26 to 32 (455 million pixels containing clouds). Results were binned and averaged according to Ls and latitude. Fig. 11a) shows the climatology of WIC estimated from the OMEGA data using our empirical relationship between ICI and M. Clearly visible is the aphelion seasonal cloud belt which peaks near Ls 90°. This matches water ice aerosol climatologies derived from other instruments, such as the TES (Smith, 2004), THEMIS (Smith, 2009), and the Mars Express Ultraviolet and Infrared Atmospheric Spectrometer (SPICAM) (Mateshvili et al., 2009; Willame et al., 2017). These climatologies have been made for water ice optical depth, are generally in agreement with one another, and feature two prominent features: the aphelion clouds between Ls 30° and 180°, and between 30°S and 30°N; and the polar hoods, along the northern and southern limits of coverage. The climatologies derived from TES and THEMIS have very good coverage, but view less of the polar hoods than what we show in Fig. 11, while those derived from SPICAM are very sparse. In the fringes of the polar hoods observed by TES and THEMIS, the opacity of the water ice clouds is equal to those over the aphelion belt, while we have observed clouds with greater mass in the polar hoods than in the aphelion belt. This was also observed by SPICAM, though with limited coverage.

The magnitude of the WIC within the aphelion cloud belt is between 1.2–1.6 pr. µm, but climbs above 2.5 pr. µm in the polar hoods, where the WIC is generally between 1.5–2.5 pr. µm. It must be noted that the polar hoods are only covered on the fringes of the spatial domain of OMEGA observations, fewer data points are used in the climatology, resulting in higher standard errors for these points. Madeleine et al. (2012) reported WIC values

between 2–3.5 pr. µm for single OMEGA pixels over the aphelion belt, and noted that this result was higher than previous measurements presented by Benson et al. (2003) and Mateshvili et al. (2007), who reported WIC values of 0.07–2.1 pr. µm and 1.35–1.8 pr. µm, respectively.

The standard deviations of the climatology pixels are distributed between 0.1–0.3 pr. µm over the majority of the covered area, as shown in Fig. 11b). Higher standard deviations, between 0.2–0.7 pr. µm, are seen in regions where clouds may be present, such as the aphelion belt. Outliers, with standard deviations between 1–2 pr. µm, appear on the southern edge of the OMEGA limit near the south polar hood (Ls 30°–160°). These pixels correspond to WIC enhancements in Fig. 11 (dark red and orange), and suffer below average sample sizes ($< 5,000$ compared to a mean of 50,000). The enhancements seen in the north polar hood (Ls $> 280°$) have nominal sample sizes ($> 10,000$) and low standard deviations (0.25–0.75 pr. µm). The standard errors for the WIC climatology pixels shown in Fig. 11 are distributed between 0.0002–0.0015 pr. µm.

A detailed analysis of the ICI distribution and climatology has already been performed by Szantai et al. (2017b, 2019), with a focus on examining the extent of cloud cover and the diurnal cycle of water-ice clouds. That work compared the ICI and the percentage of cloudy pixels for an OMEGA observation to the integrated water ice optical thickness derived from TES (Smith, 2004) and the integrated water ice column from the MCD (Forget et al., 1999; Navarro et al., 2014). OMEGA water ice and cloudiness indicators were temporally averaged onto maps (latitude and longitude) and were compared to spatially and temporally collocated TES and MCD data.

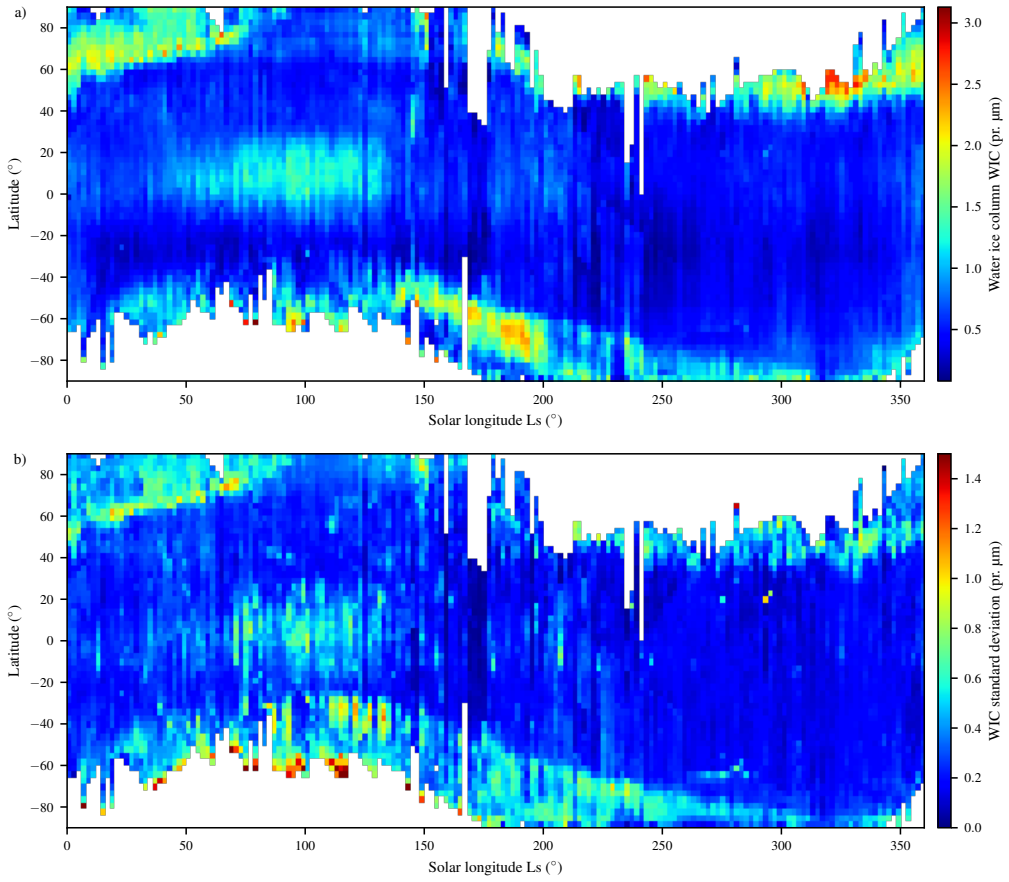

Figure 11: a) Water-ice column (WIC) climatology estimated from OMEGA ICI data. Data shown are for all years (MY 26–32) restricted to local daytime(06:00 to 20:00). Data are binned in a grid of 2° Ls and 3° latitude. Panel b) shows the corresponding standard deviation of the WIC computed for each bin.

7. Constraining $r_{\mathbf{eff}}$

A very large number of the analyzed pixels resulted in higher than expected values of r_{eff} (e.g., with respect to Wolff and Clancy, 2003; Fedorova et al., 2014), as seen in Fig. 5a. A large effort was dedicated to understand-

ing these results, to determine whether they were real and truly reflected the state of the atmosphere, to diagnose what elements of the spectral modelling and fitting were responsible, and to establish whether the retrieval could be modified or constrained to reduce their occurrence.

While some results are related to surface features, as seen in Fig.s 6 and 7, it is difficult to quantify their contribution to Fig. 5a without a method for identifying cratering and cliffs in the OMEGA images. The slope of the surface at a given pixel centre can be computed from the MOLA data, but due the spatial resolution, the maximum slopes found within our data set are only around 10–11°, very few pixels lie on slopes greater than a few degrees, and we found no correlation between pixels with steep slopes and high-$r_{\rm eff}$ retrievals or χ^2.

To investigate these high-$r_{\rm eff}$ results, we looked for correlations between each parameter in the retrieval results ($r_{\rm eff}$, $\tau_{\rm i}$, and χ^2) and any other properties of the pixels. For every property we investigated, we found poor correlations between it and our results. There are no clear rules that can be applied to the data to reject a pixel's result. We can obtain a good fit and a reasonable result when a pixel is abnormal in some aspect, while having a failed retrieval, either a very poor fit or a very high $r_{\rm eff}$, when all aspects are nominal.

The properties of an OMEGA pixel that we investigated are: the surface elevation, the surface slope, the surface temperature, the ICI, the mean retrieved surface albedo (at spectral points used, below 2.5 µm), the mean level of the cloudy spectrum (at spectral points used, below 2.5 µm), the difference between the mean spectrum levels, the H_2O band depth at 1.5 µm

(Langevin et al., 2007), the dust opacity in the cloudy spectrum, the dust opacity in the cloud-free spectrum used to retrieve surface albedo, the ratio of dust opacities between the cloudy and cloud-free spectra, the spatial resolution of the pixel, the spatial resolution of the cloud-free pixel, the ratio of the spatial resolutions, the maximum of the digital number (raw OMEGA signal), phase angle, and the incidence angle. No trends were found for the majority of the listed properties, but some provided insight into the limitations of our retrieval. We found correlations between high-r_{eff} results and the ICI, which was expected, and surface elevation, which was coincidental. The following four properties, which are all related to one another, may contribute to unreliable retrievals: the dust opacity in the cloud-free pixels, the mean retrieved surface albedo, the difference between the mean albedo and the mean spectrum level, and the ratio of dust opacities between the cloudy and cloud-free pixels.

Large ICI values infer that cloud cover is thin, which limits the information content of the data in our retrieval. As the amount of water-ice in the atmosphere decreases, so too does our ability to accurately determine its properties. Therefore, we did find that the occurrence of high-r_{eff} retrievals tends to increase with the ICI, but the variability of retrieval results for thin clouds is still very large, and we must understand what other factors are at play.

The appearance of a correlation between high-r_{eff} retrievals and surface elevation is coincidental. We observed an increase in high-r_{eff} values at elevations near zero, but that was only because the majority of observation occur at low elevations. Observations made at higher elevations tend to be

of thicker clouds due to cloud formation processes near the Tharsis volcanoes (e.g., Pearl et al., 2001; Benson et al., 2003; Smith, 2004), where the majority of our data comes from.

The correlation between r_{eff} and the ratio of dust opacities in the cloudy and cloud-free spectra is also coincidental. In both cases, the dust opacity is frequently low and their ratio is close to unity. Thus we see many high-r_{eff} retrievals with this ratio, but we see the same thing for all values of r_{eff}.

We searched for aspects of the a priori multi-spectral surface albedo, which we established that our retrievals are critically dependent on, that systematically lead to unrealistic results. We found that as the dust opacity of the cloud-free pixels used in the surface albedo retrieval increases, the retrieved albedo values can as well. Indeed, the presence of dust in the atmosphere decreases the reflectance factor of bright surfaces and increases that of dark surfaces (Vincendon et al., 2007). Therefore, when dust is removed from the observed spectra, the brightness factor increases for bright regions and decreases for dark regions. To retrieve albedo, OMEGA observations were chosen to have low dust opacities and to be cloud-free, but dust is always present to a small extent and is generally between 0.04–0.45. Dust opacities used in the albedo retrieval come from the climatology of Montabone et al. (2015) and tend to be fairly homogeneous over the area covered by an OMEGA observation. There is more variability in the levels of the resulting multi-spectral surface albedo among the pixels in an OMEGA image cube than in the dust opacities used, due to intrinsic variations in the properties of the surface. High levels of dust optical depth do not necessarily imply high values for the retrieved surface albedos.

7.1. High-r_{eff} Case Studies

To further explore these high-r_{eff} results, we looked at several distinct cases, or groupings, within the data. Two such groups were the set of OMEGA image cubes with the highest percentage of high-r_{eff} results, and the sets of retrievals with the highest, and lowest, resulting values of r_{eff}.

In the first case we calculated the ratio of retrievals with $r_{\mathrm{eff}} < 7$ µm to those with $r_{\mathrm{eff}} > 7$ µm, and took the ten OMEGA observations that had the lowest ratio and that had more than 1000 pixels analyzed (without applying data quality cuts). These observations are: 0902_5 (MY 27, Ls 95.3°), 0931_5 (MY 27, Ls 98.9°), 0942_5 (MY 27, Ls 100.3°), 0942_6 (MY 27, Ls 100.3°), 1022_6 (MY 27, Ls 110.4°), 1030_7 (MY 27, Ls 111.4°), 1055_6 (MY 27, Ls 114.7°), 3305_3 (MY 28, Ls 89.0°), 3316_3 (MY 28, Ls 90.4°), and 8371_1 (MY 28, Ls 111.7°). These ten observations collectively have 41019 analyzed pixels, but account for about half of the results with $r_{\mathrm{eff}} > 7$ µm in Fig. 5a. Histograms of the retrieved r_{eff} values for these observations are shown in Fig. 12a, and they infer that the cloud formations they represent are predominantly made up of very large water-ice particles. Fig. 12b shows a histogram of the combined data from Fig. 12a, compared with the entire data set (same as Fig. 5a).

We compared the properties of this group of pixels to the whole data set and found that most properties, such as ICI, phase angle, incidence angle, surface temperature, elevation, H_2O band depths, spatial resolutions, etc., were average. However, two properties stood out: the dust opacity in the cloudy observations, and the dust opacity in the cloud-free observation used to retrieve surface albedo. Fig. 12c shows a histogram of the dust opacities

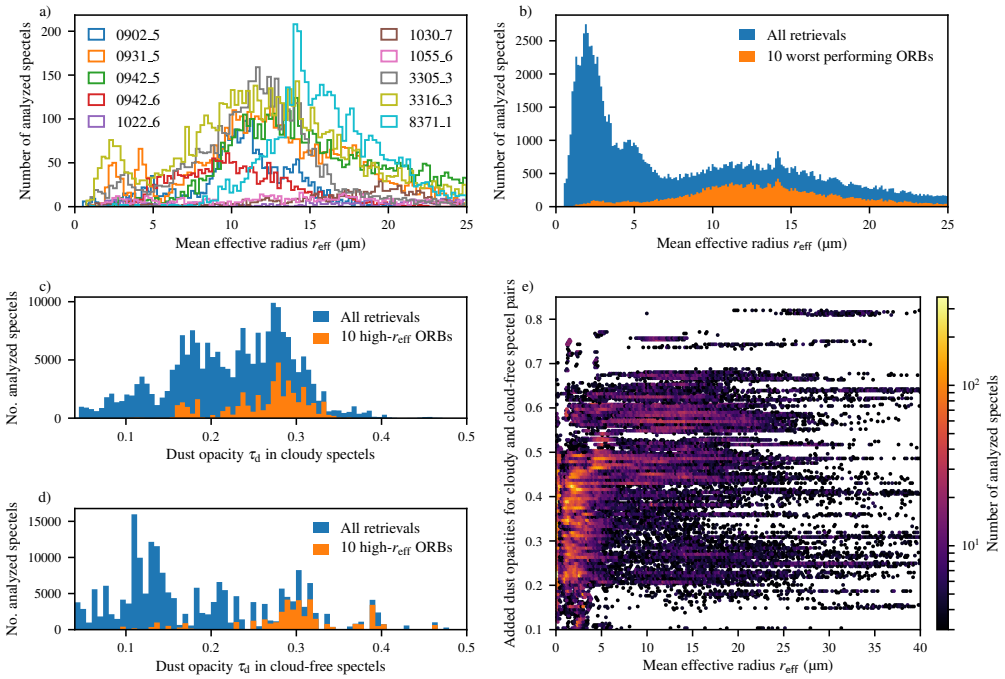

Figure 12: Results from a case study of the ten OMEGA observations returning the highest proportions of high-r_{eff} retrievals. Panel a) shows histograms of retrieved r_{eff} for each of the ten observations, and panel b) compared histograms of r_{eff} after combining all ten observations in panel a) to the entire data set. Panel c) and d) are the same as panel b), but comparing a) the dust opacity used for the cloudy pixels used in the r_{eff} retrievals, and b) the dust opacity in the cloud-free pixels used in the surface albedo retrieval. Panel e) shows the parameter space between the retrieved r_{eff} and the sum of the dust opacities used in the r_{eff} retrieval and the surface albedo retrieval.

719 from the cloud-free pixels used for albedo retrievals used here, and Fig. 12d
720 shows a histogram of the dust opacities from the cloudy pixels. These fig-
721 ures also show the contributions from the ten observations identified in this
722 investigation. The dust present in both the cloudy and cloud-free spectra is
723 above average

What we learned from this analysis was that we can use surface albedos retrieved when the dust opacity is elevated, and we can successfully retrieve water-ice cloud properties when the dust opacity is elevated, but we cannot perform retrievals when the dust opacity is elevated in both the cloudy and cloud-free OMEGA observations. A generalization of this observation is inferred from Fig. 12e, which shows the relationship between the retrieved r_{eff} and the sum of the dust opacities used for the albedo and cloud properties retrievals. While high-r_{eff} retrievals may occur in any dust situation, when the sum of the dust opacities is above 0.5, the retrieval favours $r_{\mathrm{eff}} > 5\,\mu\mathrm{m}$.

In a second case study, we compared groups of OMEGA pixels that were distinguished by the magnitude of their retrieved r_{eff} values. Within each grouping, we compared different properties and calculated the mean spectrum and mean multi-spectral albedo for hundreds of pixels. In general, we found that the level of the baseline of the spectra tended to be related to high-r_{eff} results. The baseline is affected by the intrinsic surface albedo as well as dust suspended in the atmosphere. If the albedo was measured with a dust-free atmosphere, then dust in the cloudy observation can be decoupled from the water ice signature. However, if dust absorption contaminated the albedo measurement, then dust in the cloudy spectrum is not fully corrected for, resulting in compensation in the r_{eff} and τ_{i} retrieval.

Three groups of particular interest were pixels with: $1\ \mu\mathrm{m} < r_{\mathrm{eff}} < 3\ \mu\mathrm{m}$, representing retrievals with expected values; $16\ \mu\mathrm{m} < r_{\mathrm{eff}} < 25\ \mu\mathrm{m}$, representing retrievals with un-physically large results; and $r_{\mathrm{eff}} > 40\ \mu\mathrm{m}$, representing failed retrievals (see Fig. 5a). A striking feature of the last group is in the ICIs data. It is made up predominantly of pixels with very thin clouds

and high-ICI. In this region, the retrieval is unreliable as the water-ice information content in the spectra is minimal. By comparing these groups, we are able to see that there is a strong correlation between the shape of the spectrum and the result.

Fig. 13a shows averaged spectra representing the following criteria: low r_{eff}, with $2.3\,\mu\mathrm{m} \leq r_{\mathrm{eff}} \leq 2.8\,\mu\mathrm{m}$ and $1.1 \leq \tau_{\mathrm{i}} \leq 1.7$; and high r_{eff}, with $40\,\mu\mathrm{m} \leq r_{\mathrm{eff}} \leq 48\,\mu\mathrm{m}$, $0 \leq \tau_{\mathrm{i}} \leq 1$, and $\chi^2 < 2000$. The means of their corresponding multi-spectral surface albedo are also shown. The difference is striking between the two groups. Because this large difference is also reflected in the albedo data, which are taken from different OMEGA observations over the same location, we believe that these data are not anomalous and that the spectra reflect aspects of the surface not accounted for by the retrieval. This could be strong shadowing, or steep surfaces around crater rims (Vincendon et al., 2007).

To further investigate these data, we estimated a baseline for the C-channel portion of the spectra by computing the average value of the points used in the retrieval below 2.5 µm.Fig. 13b shows the relationship between the mean baseline and the retrieved r_{eff}. There are three large clusters: the data with expected r_{eff} values, and the majority, lies below 7 μ; there is a large group between 7–25 μ, explored above and in Fig. 12; and there is a group covering the entire r_{eff} range, but with baselines below 0.37. This group of pixels, with low baseline and high-r_{eff} results, tends to have lower than average maximum digital number (the raw OMEGA signal strength is lower than average), and lower than average surface elevation. These pixels are most likely affected by shadowing on the surface, which our model does

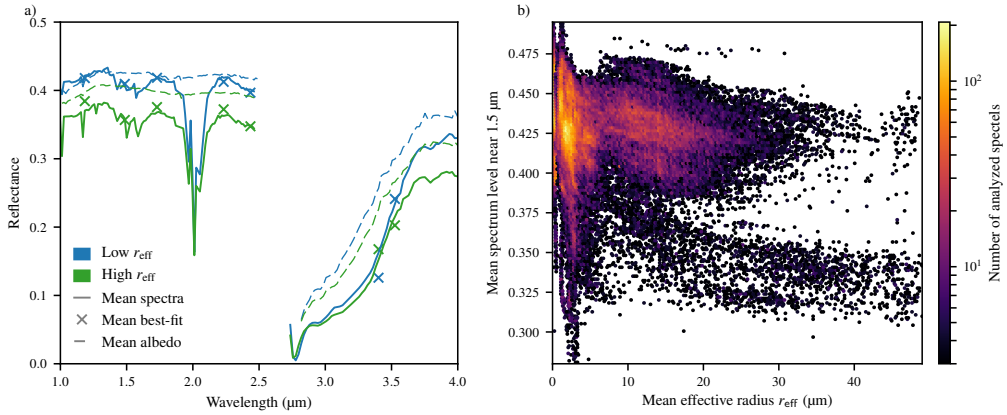

Figure 13: Case study for extremely large retrieved r_{eff}. Panel a) shows the means of 1000 randomly selected spectra that resulted in retrieval results that satisfied: low r_{eff} (blue) $2.3\,\mu\text{m} \leq r_{\text{eff}} \leq 2.8\,\mu\text{m}$, $1.1 \leq \tau_{\text{i}} \leq 1.7$; and high r_{eff} (green) $40\,\mu\text{m} \leq r_{\text{eff}} \leq 48\,\mu\text{m}$, $0 \leq \tau_{\text{i}} \leq 1$, and $\chi^2 < 2000$. Also shown are the means of the multi-spectral albedo data used in each retrieval, and the mean best-fit results. Panel b) shows the parameter space of the retrieved r_{eff} and the baseline of the C-channel spectra, which is defined as the mean of the spectral points at 1.18, 1.49, 1.73, 2.23, and 2.43 μm.

not accommodate for.

7.2. Mitigation

We made several attempt to alter the retrieval method to try to get more realistic results from all the analyzed pixels. The objective was to affect the the χ^2 minimization for retrievals with low values of τ_{i} in order to favour a position in the phase space with equal mass, but lower r_{eff} (e.g., see Fig. 2b). While some methods returned some desirable results, they came at the cost of impacting our already reliable retrievals, made with a robust method, in negative ways. In the absence of a precise method of identifying low-quality results, and the desire to maintain a consistent data product, we have not

incorporated any retrievals derived from these modifications into our data product. Instead, we provide our understanding of the limitation of the retrieval and the causes of high r_{eff} results, which may be real in some cases.

We varied the number of parameters, and the position of the spectral points we used in the retrieval. These tests resulted in surprising results that reflected water vapour as well as ice aerosols. We included a third free parameter, such as the dust opacity, or a multiplicative or additive parameter to modify the albedo data. The spectra, especially when using a limited number of spectral points, do not support this many degrees of freedom. The computation of the χ^2 was modified with a parameter to favour a r_{eff} of 2 or 2.2, but this had a negative impact on retrievals which already returned $r_{\text{eff}} < 7$. We attempted to remove the signature of CO_2 gas in the spectra prior to the retrieval, but this resulted in worse fits, higher χ^2, and more convergence failures.

We also tried to use the ICI to constrain the r_{eff} retrievals by applying the relationship presented in Section 6.3 to the degenerate data. For retrievals with a r_{eff} above a threshold (e.g., 7 or 9 µm), we assume that the τ_{i} retrieval is more accurate than that of r_{eff}. We use the ICI to compute the empirical column mass, then use equation 1 to compute a new value for r_{eff} from the retrieved τ_{i} and the estimated M. While this method works and does not have an impact on nominal r_{eff} retrievals, there is a lack of variability in the r_{eff} and τ_{i} parameter space after applying such a simple estimation to constrain r_{eff}. The variability we see in Fig. 9a, for example, reflects physical aspects of the OMEGA spectra. This method imposes a forced smoothing on the high-r_{eff} data, making it difficult to re-combine the constrained data

with the original data.

8. Conclusions

In this manuscript we have presented a novel, statistical approach to the retrieval of physical cloud properties from OMEGA spectral images. We have applied that retrieval to a large subset of OMEGA data motivated by the availability of improved prior information, especially maps of multi-spectral surface albedo derived from co-located, cloud-free OMEGA observations. The average water-ice aerosol size in low-latitude cloud formations is 2.2 µm (standard deviation of 0.83). One of our objectives was to examine the spatial distribution of cloud properties in single cloud formations. However, this is challenged by the limitations of the shape of the OMEGA observations (often only 16 or 32 pixels wide) and the size of the subset of OMEGA data analyzed (limited by the lifetime of the OMEGA C-channel detector and the amount of processed albedo data). We also found that applying the retrieval over many pixels of varying cloud thickness reaches the limitations of the technique and the water-ice information content in the spectra.

The retrieved parameters, water-ice optical depth, τ_{i}, and mean effective radius, r_{eff}, closely conform to an inverse relationship (see equation 1 and Fig. 9a). We found that for optically thin clouds, it is difficult to get an accurate retrieved r_{eff} value, and that there is some degeneracy in the retrieval parameter space (see Fig. 2b). A large effort was made to understand retrievals with higher than expected r_{eff}. We believe that these results may be real in some cases, but that several aspects may lead to unreliable results, such as the impact of dust in both of the co-located OMEGA observations

used to retrieve surface albedo and cloud properties, or OMEGA spectra with uncharacteristically low reflectances.

We have found an empirical relationship between the ice cloud index, ICI, and the column mass of water ice, M, or the water ice column, WIC. The temporal and spatial extent of the ICI data is much larger than those of the cloud properties retrievals, and work is being done to study the climatology of clouds using the ICI data, and to compare them to other data sets. We have applied our empirical relationship to the entire OMEGA data set and presented a climatology, binned by latitude and solar longitude, of derived WIC from daytime OMEGA observations covering Mars years 26–32 (Fig. 11). The primary features seen are the aphelion cloud belt centred on LS 90°, and the polar hoods. These are both observed in other water-ice aerosol climatologies. WIC values range from 1.2–1.6 pr. µm over the aphelion belt, and 1.5–2.5 pr. µm over the poles. Future work will expand the retrieved surface albedo and cloud properties data sets, focusing on increasing the number of results for pixels with ICI < 0.35 to better constrain our empirical relationship and the derived WIC climatology.

The results of this work have been uploaded to the ESA Planetary Science Archive at open.esa.int/esa-planetary-science-archive/ in a format conforming to the Planetary Data System (Version 4).

9. Acknowledgements

This work has received funding from the European Union's Horizon 2020 Programme (H2020-COMPET-08-2014) under grant agreement UPWARDS-633127. It was performed in support of UPWARDS work package 4: under-

standing Mars water cycle and clouds by combining data & models; Task 4.1: Mapping cloud optical depth and particle size using Mars Express OMEGA imaging spectrometer data (CNRS,INAF). The retrieval algorithm was originally developed by J.-B. Madeleine and uses the DISORT radiative transfer code. We thank our colleagues who developed the prior information used: Anna Geminale and her team generated the albedo data, Luca Montabone generated the dust climatology, Joachim Audouard and Andre Szantai provided ICI maps and databases, and LMD maintains the Mars Climate Database.

Audouard, J., Poulet, F., Vincendon, M., Bibring, J.-P., Forget, F., Langevin, Y., Gondet, B., May 2014. Mars surface thermal inertia and heterogeneities from OMEGA/MEX. Icarus 233, 194–213.

Batson, R. M., Bridges, P. M., Inge, J. L., 1979. Atlas of Mars : the 1:5,000,000 map series. Scientific and Technical Information Branch, NASA, Washington, D.C.

Benson, J. L., Bonev, B. P., James, P. B., Shan, K. J., Cantor, B. A., Caplinger, M. A., Sep. 2003. The seasonal behavior of water ice clouds in the Tharsis and Valles Marineris regions of Mars: Mars Orbiter Camera Observations. Icarus 165, 34–52.

Bibring, J.-P., Soufflot, A., Berthé, M., Langevin, Y., Gondet, B., Drossart, P., Bouyé, M., Combes, M., Puget, P., Semery, A., Bellucci, G., Formisano, V., Moroz, V., Kottsov, V., Bonello, G., Erard, S., Forni, O., Gendrin, A., Manaud, N., Poulet, F., Poulleau, G., Encrenaz, T., Fouchet, T., Melchiori, R., Altieri, F., Ignatiev, N., Titov, D., Zasova, L., Coradini, A.,

881 Capacionni, F., Cerroni, P., Fonti, S., Mangold, N., Pinet, P., Schmitt, B.,
882 Sotin, C., Hauber, E., Hoffmann, H., Jaumann, R., Keller, U., Arvidson,
883 R., Mustard, J., Forget, F., Aug. 2004. OMEGA: Observatoire pour la
884 Minéralogie, l'Eau, les Glaces et l'Activité. In: Wilson, A., Chicarro, A.
885 (Eds.), Mars Express: the Scientific Payload. Vol. 1240 of ESA Special
886 Publication. pp. 37–49.

887 Bohren, C. F., Huffman, D. R., Mar. 1983. Absorption and Scattering of Light
888 by Small Particles. Wiley-VCH Verlag GmbH & Co. KGaA, Weinheim,
889 Germany.

890 Christensen, P. R., Zurek, R. W., Jun. 1984. Martian north polar hazes
891 and surface ice - Results from the Viking Survey/Completion mission. J.
892 Geophys. Res. 89, 4587–4596.

893 Clancy, R. T., Lee, S. W., Gladstone, G. R., McMillan, W. W., Rousch, T.,
894 Mar. 1995. A new model for Mars atmospheric dust based upon analysis
895 of ultraviolet through infrared observations from Mariner 9, Viking, and
896 PHOBOS. J. Geophys. Res. 100, 5251–5263.

897 Clancy, R. T., Wolff, M. J., Christensen, P. R., Sep. 2003. Mars aerosol
898 studies with the MGS TES emission phase function observations: Opti-
899 cal depths, particle sizes, and ice cloud types versus latitude and solar
900 longitude. J. Geophys. Res. 108 (E9), 5098.

901 Curran, R. J., Conrath, B. J., Hanel, R. A., Kunde, V. G., Pearl, J. C., Oct.
902 1973. Mars: Mariner 9 Spectroscopic Evidence for H_2O Ice Clouds. Science
903 182, 381–383.

Fedorova, A. A., Montmessin, F., Rodin, A. V., Korablev, O. I., Määttänen, A., Maltagliati, L., Bertaux, J.-L., Mar. 2014. Evidence for a bimodal size distribution for the suspended aerosol particles on Mars. Icarus 231, 239–260.

Forget, F., Hourdin, F., Fournier, R., Hourdin, C., Talagrand, O., Collins, M., Lewis, S. R., Read, P. L., Huot, J.-P., Oct. 1999. Improved general circulation models of the Martian atmosphere from the surface to above 80 km. J. Geophys. Res. 104, 24155–24176.

Geminale, A., Grassi, D., Altieri, F., Serventi, G., Carli, C., Carrozzo, F. G., Sgavetti, M., Orosei, R., D'Aversa, E., Bellucci, G., Frigeri, A., Jun. 2015. Removal of atmospheric features in near infrared spectra by means of principal component analysis and target transformation on Mars: I. Method. Icarus 253, 51–65.

Glenar, D. A., Samuelson, R. E., Pearl, J. C., Bjoraker, G. L., Blaney, D., Feb. 2003. Spectral imaging of martian water ice clouds and their diurnal behavior during the 1999 aphelion season ($L_s = 130°$). Icarus 161, 297–318.

Guzewich, S. D., Smith, M. D., Wolff, M. J., Dec. 2014. The vertical distribution of Martian aerosol particle size. J. Geophys. Res. 119, 2694–2708.

Haberle, R. M., Clancy, R. T., Forget, F., Smith, M. D., Zurek, R. W., Mar. 2017. The atmosphere and climate of Mars. Cambridge Planetary Science. Cambridge University Press.

Ignatiev, N. I., Grassi, D., Zasova, L. V., Aug. 2005. Planetary Fourier spec-

926 trometer data analysis: Fast radiative transfer models. Planet. Space Sci.
927 53, 1035–1042.

928 James, P. B., Bell, J. F., Clancy, R. T., Lee, S. W., Martin, L. J., Wolff,
929 M. J., Aug. 1996. Global imaging of Mars by Hubble space telescope during
930 the 1995 opposition. J. Geophys. Res. 101, 18883–18890.

931 Langevin, Y., Bibring, J.-P., Montmessin, F., Forget, F., Vincendon, M.,
932 Douté, S., Poulet, F., Gondet, B., Jul. 2007. Observations of the south
933 seasonal cap of Mars during recession in 2004-2006 by the OMEGA
934 visible/near-infrared imaging spectrometer on board Mars Express. J. Geo-
935 phys. Res. 112, E08S12.

936 Madeleine, J.-B., Forget, F., Millour, E., Montabone, L., Wolff, M. J., Nov.
937 2011. Revisiting the radiative impact of dust on Mars using the LMD
938 Global Climate Model. J. Geophys. Res. 116 (E15), E11010.

939 Madeleine, J.-B., Forget, F., Spiga, A., Wolff, M. J., Montmessin, F., Vincen-
940 don, M., Jouglet, D., Gondet, B., Bibring, J.-P., Langevin, Y., Schmitt, B.,
941 May 2012. Aphelion water-ice cloud mapping and property retrieval using
942 the OMEGA imaging spectrometer onboard Mars Express. J. Geophys.
943 Res. 117, E00J07.

944 Mateshvili, N., Fussen, D., Vanhellemont, F., Bingen, C., Dekemper, E.,
945 Loodts, N., Tetard, C., Jul. 2009. Water ice clouds in the Martian atmo-
946 sphere: Two Martian years of SPICAM nadir UV measurements. Planet.
947 Space Sci. 57, 1022–1031.

948 Mateshvili, N., Fussen, D., Vanhellemont, F., Bingen, C., Dodion, J.,
949 Montmessin, F., Perrier, S., Dimarellis, E., Bertaux, J.-L., Jul. 2007. Mar-
950 tian ice cloud distribution obtained from SPICAM nadir UV measure-
951 ments. J. Geophys. Res. 112, E07004.

952 Millour, E., Forget, F., Spiga, A., Navarro, T., Madeleine, J.-B., Montabone,
953 L., Pottier, A., Lefevre, F., Montmessin, F., Chaufray, J.-Y., Lopez-
954 Valverde, M. A., Gonzalez-Galindo, F., Lewis, S. R., Read, P. L., Huot,
955 J.-P., Desjean, M.-C., MCD/GCM development Team, Oct. 2015. The
956 Mars Climate Database (MCD version 5.2). European Planetary Science
957 Congress 10, EPSC2015–438.

958 Mishchenko, M. I., Travis, L. D., Mackowski, D. W., May 1996. T-matrix
959 computations of light scattering by nonspherical particles: a review. J.
960 Quant. Spectrosc. Radiat. Transfer 55, 535–575.

961 Montabone, L., Forget, F., Millour, E., Wilson, R. J., Lewis, S. R., Cantor,
962 B., Kass, D., Kleinböhl, A., Lemmon, M. T., Smith, M. D., Wolff, M. J.,
963 May 2015. Eight-year climatology of dust optical depth on Mars. Icarus
964 251, 65–95.

965 Navarro, T., Madeleine, J.-B., Forget, F., Spiga, A., Millour, E., Montmessin,
966 F., Määttänen, A., Jul. 2014. Global climate modeling of the Martian water
967 cycle with improved microphysics and radiatively active water ice clouds.
968 J. Geophys. Res. 119, 1479–1495.

969 Parker, D. C., Beish, J. D., Troiani, D. M., Joyce, D. P., Hernandez, C. E.,

970 Mar. 1999. Telescopic Observations of Mars, 1996-1997: Results of the
971 Marswatch Program. Icarus 138, 3–19.

972 Pearl, J. C., Smith, M. D., Conrath, B. J., Bandfield, J. L., Christensen,
973 P. R., Jun. 2001. Observations of Martian ice clouds by the Mars Global
974 Surveyor Thermal Emission Spectrometer: The first Martian year. J. Geo-
975 phys. Res. 106, 12325–12338.

976 Petrova, E., Keller, H. U., Markiewicz, W. J., Thomas, N., Wuttke, M. W.,
977 Oct. 1996. Ice hazes and clouds in the Martian atmosphere as derived from
978 the Phobos/KRFM data. Planet. Space Sci. 44, 1163–1176.

979 Pollack, J. B., Ockert-Bell, M. E., Shepard, M. K., Mar. 1995. Viking Lander
980 image analysis of Martian atmospheric dust. J. Geophys. Res. 100, 5235–
981 5250.

982 Rannou, P., Perrier, S., Bertaux, J.-L., Montmessin, F., Korablev, O.,
983 Rébérac, A., Sep. 2006. Dust and cloud detection at the Mars limb with
984 UV scattered sunlight with SPICAM. J. Geophys. Res. 111, E09S10.

985 Smith, M. D., Jan. 2004. Interannual variability in TES atmospheric obser-
986 vations of Mars during 1999-2003. Icarus 167, 148–165.

987 Smith, M. D., Aug. 2009. THEMIS observations of Mars aerosol optical depth
988 from 2002-2008. Icarus 202, 444–452.

989 Smith, M. D., Wolff, M. J., Clancy, R. T., Kleinböhl, A., Murchie, S. L.,
990 Feb. 2013. Vertical distribution of dust and water ice aerosols from CRISM
991 limb-geometry observations. J. Geophys. Res. 118, 321–334.

Smith, P. H., Lemmon, M., Apr. 1999. Opacity of the Martian atmosphere measured by the Imager for Mars Pathfinder. J. Geophys. Res. 104, 8975–8986.

Stamnes, K., Tsay, S.-C., Jayaweera, K., Wiscombe, W., Jun. 1988. Numerically stable algorithm for discrete-ordinate-method radiative transfer in multiple scattering and emitting layered media. Appl. Opt. 27, 2502–2509.

Szantai, A., Audouard, J., Forget, F., Madeleine, J.-B., Pottier, A., Millour, E., Gondet, B., Langevin, Y., Bibring, J.-P., Jan. 2017a. Construction of a 4D Water Ice Cloud Database from Mars Express / OMEGA Observations - Derivation of the Diurnal Martian Cloud Life Cycle. In: Forget, F., Millour, E. (Eds.), The Mars Atmosphere: Modelling and observation. p. 3208.

Szantai, A., Audouard, J., Forget, F., Madeleine, J.-B., Pottier, A., Millour, E., Gondet, B., Langevin, Y., Bibring, J.-P., Sep. 2017b. Martian cloud coverage and diurnal cloud life cycle derived from gridded Mars/Express OMEGA data. In: European Planetary Science Congress. Vol. 11. pp. EPSC2017–879.

Szantai, A., Audouard, J., Forget, F., Olsen, K. S., Millour, E., Madeleine, J.-B., Pottier, A., Gondet, B., Langevin, Y., Bibring, J.-P., 2019. Martian cloud climatology and life cycle extracted from Mars Express OMEGA spectral images. J. Quant. Spectrosc. Radiat. Transfer, this issue.

Tamppari, L. K., Zurek, R. W., Paige, D. A., Jul. 2003. Viking-era diurnal water-ice clouds. J. Geophys. Res. 108, 9–1.

1015 Toon, O. B., Pollack, J. B., Sagan, C., Apr. 1977. Physical properties of
1016 the particles composing the Martian dust storm of 1971-1972. Icarus 30,
1017 663–696.

1018 Vincendon, M., Langevin, Y., Poulet, F., Bibring, J.-P., Gondet, B., Jul.
1019 2007. Recovery of surface reflectance spectra and evaluation of the optical
1020 depth of aerosols in the near-IR using a Monte Carlo approach: Application
1021 to the OMEGA observations of high-latitude regions of Mars. J. Geophys.
1022 Res. 112, E08S13.

1023 Warren, S. G., Brandt, R. E., Jul. 2008. Optical constants of ice from the
1024 ultraviolet to the microwave: A revised compilation. J. Geophys. Res.
1025 113 (D12), D14220.

1026 Whiteway, J. A., Komguem, L., Dickinson, C., Cook, C., Illnicki, M.,
1027 Seabrook, J., Popovici, V., Duck, T. J., Davy, R., Taylor, P. A., Pathak,
1028 J., Fisher, D., Carswell, A. I., Daly, M., Hipkin, V., Zent, A. P., Hecht,
1029 M. H., Wood, S. E., Tamppari, L. K., Renno, N., Moores, J. E., Lemmon,
1030 M. T., Daerden, F., Smith, P. H., Jul. 2009. Mars Water-Ice Clouds and
1031 Precipitation. Science 325, 68.

1032 Willame, Y., Vandaele, A. C., Depiesse, C., Lefèvre, F., Letocart, V.,
1033 Gillotay, D., Montmessin, F., Aug. 2017. Retrieving cloud, dust and ozone
1034 abundances in the Martian atmosphere using SPICAM/UV nadir spectra.
1035 Planet. Space Sci. 142, 9–25.

1036 Wolff, M. J., Clancy, R. T., Sep. 2003. Constraints on the size of Martian

1037 aerosols from Thermal Emission Spectrometer observations. J. Geophys.
1038 Res. 108 (E9), 5097.

1039 Wolff, M. J., Smith, M. D., Clancy, R. T., Arvidson, R., Kahre, M., Seelos,
1040 F., Murchie, S., Savijärvi, H., Jun. 2009. Wavelength dependence of dust
1041 aerosol single scattering albedo as observed by the Compact Reconnais-
1042 sance Imaging Spectrometer. J. Geophys. Res. 114, E00D04.

1043 Zasova, L., Grassi, D., Formisano, V., Maturilli, A., Aug. 2001. The Martian
1044 atmosphere in the region of the great volcanoes: Mariner 9 IRIS data
1045 revisited. Planet. Space Sci. 49, 977–992.

1046 Zasova, L. V., Formisano, V., Moroz, V. I., Bibring, J.-P., Grassi, D., Ig-
1047 natiev, N. I., Giuranna, M., Bellucci, G., Altieri, F., Blecka, M., Gnedykh,
1048 V. N., Grigoriev, A. V., Lellouch, E., Mattana, A., Maturilli, A., Moshkin,
1049 B. E., Nikolsky, Y. V., Patsaev, D. V., Piccioni, G., Ratai, M., Saggin, B.,
1050 Fonti, S., Khatuntsev, I. V., Hirsh, H., Ekonomov, A. P., Jul. 2006. Results
1051 of measurements with the Planetary Fourier Spectrometer onboard Mars
1052 Express: Clouds and dust at the end of southern summer. A comparison
1053 with OMEGA images. Cosmic Research 44, 305–316.